DARWIN, C. G. (1914*b*). *Philos. Mag.* **27**, 675-690.
EWALD, P. P. (1916*a*). *Ann. Phys. (Leipzig)*, **49**, 1-38.
EWALD, P. P. (1916*b*). *Ann. Phys. (Leipzig)*, **49**, 117-143.
EWALD, P. P. (1917). *Ann. Phys. (Leipzig)*, **54**, 519-597.
EWALD, P. P. (1962). *J. Phys. Soc. Jpn*, **17**, Supplement B-II, 48-52.
HASHIMOTO, H., HOWIE, A. & WHELAN, M. J. (1962). *Proc. R. Soc. London Ser. A*, **269**, 80-103.
HEWAT, E. A. & HUMPHREYS, C. J. (1974). *High Voltage Electron Microscopy*, edited by P. R. SWANN, C. J. HUMPHREYS & M. J. GORINGE, pp. 52-56. London and New York: Academic Press.
HIRSCH, P. B., HOWIE, A., NICHOLSON, R. B., PASHLEY, D. W. & WHELAN, M. J. (1965). *Electron Microscopy of Thin Crystals*. London: Butterworths.
HOWIE, A. (1966). *Philos. Mag.* **14**, 223-237.
HOWIE, A. (1967). *Proc. Int. Conf. Solid State Physics Research with Accelerators*, Brookhaven National Laboratory 50083 (C-52), pp. 15-29. Washington: Clearing House for Federal Scientific and Technical Information.
HOWIE, A. & WHELAN, M. J. (1961*a*). *Proc. Eur. Regional Conf. on Electron Microscopy (Delft*, 1960), Vol. 1, 181-185. Delft: de Nederlandse Vereniging voor Electronenmicroscopie.
HOWIE, A. & WHELAN, M. J. (1961*b*). *Proc. R. Soc. London Ser. A*, **263**, 217-237.
HOWIE, A. & WHELAN, M. J. (1962). *Proc. R. Soc. London Ser. A*, **267**, 206-230.
HUMPHREYS, C. J. (1972). *Philos. Mag.* **25**, 1459-1472.
HUMPHREYS, C. J. & LALLY, J. S. (1970). *J. Appl. Phys.* **41**, 232-235.
JAMES, R. W. (1948). *The Optical Principles of the Diffraction of X-rays*. London: Bell.
KLEIN, A. G. & WERNER, S. A. (1983). *Rep. Prog. Phys.* **46**, 259-335.
LAUE, M. VON (1931). *Ergeb. Exakten Naturwiss.* **10**, 133-158.
LAUE, M. VON (1949). *Acta Cryst.* **2**, 106-113.
NAGATA, F. & FUKUHARA, A. (1967). *Jpn. J. Appl. Phys.* **6**, 1233-1235.
PENDRY, J. B. (1969). *J. Phys. C*, **2**, 2273-2282.
RAUCH, H. & PETRASCHECK, D. (1978). *Topics in Current Physics*. Vol. 6: *Neutron Diffraction*, Ch. 9, pp. 303-351. Berlin, Heidelberg: Springer.
SHIRLEY, C. G. & FISHER, R. M. (1979). *Philos. Mag.* A**39**, 91-117.
SMART, D. J. & HUMPHREYS, C. J. (1978). *Electron Diffraction 1927-1977. Inst. Phys. Conf. Ser.* No. 41, pp. 145-149. London: The Institute of Physics.
TAKAGI, S. (1962). *Acta Cryst.* **15**, 1311-1312.
TAUPIN, D. (1964). *Bull. Soc. Fr. Minéral. Cristallogr.* **87**, 469-511.
THOMAS, L. E., SHIRLEY, C. G., LALLY, J. S. & FISHER, R. M. (1974). *High Voltage Electron Microscopy*, edited by P. R. SWANN, C. J. HUMPHREYS & M. J. GORINGE, pp. 38-47. London and New York: Academic Press.
UYEDA, R. (1968). *Acta Cryst.* A**24**, 175-181.
WATENABE, D., UYEDA, R. & FUKUHARA, A. (1968). *Acta Cryst.* A**24**, 580-581.
WATENABE, D., UYEDA, R. & KOGISO, M. (1968). *Acta Cryst.* A**24**, 249-250.
WHELAN, M. J. (1975). *Advances in Electronics and Electron Physics*, Vol. 39, edited by L. MARTON, pp. 1-72. New York: Academic Press.
WHELAN, M. J. & HIRSCH, P. B. (1957*a*). *Philos. Mag.* **2**, 1121-1142.
WHELAN, M. J. & HIRSCH, P. B. (1957*b*). *Philos. Mag.* **2**, 1303-1324.

Acta Cryst. (1986). A**42**, 501-510

Observations of Borrmann–Lehmann Interference Patterns with Synchrotron Radiation

BY A. R. LANG AND G. KOWALSKI*

H. H. Wills Physics Laboratory, University of Bristol, Tyndall Avenue, Bristol BS8 1TL, England

A. P. W. MAKEPEACE

Department of Physiology, School of Medicine, University of Bristol, Bristol BS8 1TD, England

AND M. MOORE

Department of Physics, Royal Holloway and Bedford New College, Egham Hill, Egham, Surrey TW20 0EX, England

(*Received* 7 *February* 1986; *accepted* 2 *May* 1986)

Abstract

The intrabranch interference effects expected under Laue-Bragg diffraction conditions [Saka, Katagawa & Kato (1972). *Acta Cryst.* A**28**, 102-113, 113-120] and first studied experimentally under high-absorption conditions by Borrmann & Lehmann [*Crystallography and Crystal Perfection* (1963), edited by G. N. Ramachandran, pp. 101-108. London and New York: Academic Press] have been investigated in the moderate ($\mu_0 t = 1{\cdot}6$) and low ($\mu_0 t = 0{\cdot}47$) absorption cases with Cu $K\alpha_1$ and with synchrotron radiation of wavelengths 1·5 and 1·0 Å. Borrmann-Lehmann fringe patterns have been recorded with σ-mode and π-mode polarizations alone, utilizing the linearly polarized nature of synchrotron radiation. Specimens of natural diamonds possessing faces polished parallel to {100} and {110} were studied. The 220 reflection was recorded with the Laue entrance

* On leave from Institute of Experimental Physics, University of Warsaw, Poland.

0108-7673/86/060501-10$01.50

surface of {100} type and the Bragg-diffracting planes and internally reflecting Bragg surface oriented orthogonal to the entrance surface. Fringes of high visibility were obtained, even from specimens showing significant X-ray topographic evidence of lattice imperfections, but the fringe spacings observed wre extremely sensitive to lattice distortions. Measurements of F_{220} from Borrmann-Lehmann fringe spacings gave values much in error, worse with the shorter wavelength. Borrmann-Lehmann fringe-spacing measurement is advocated as a sensitive test of lattice perfection.

1. Introduction

The roles played by the bounding surfaces of a crystal in dynamical and in kinematical diffraction theory may be contrasted. According to kinematical theory, the crystal shape determines the variation of diffracted intensity with glancing angle (the diffraction line profile) but does not affect the integrated intensity (which depends only on the crystal volume, so long as absorption can be neglected). On the other hand, when dynamical diffraction theory applies, the strength of Bragg-diffracted rays is strongly dependent upon the geometrical shape of the crystal: partial or total reflection may occur, and the intensity of Bragg-diffracted rays generally varies in an oscillatory manner depending upon the trajectory between X-ray entrance and exit surfaces. The best known oscillations are those of *Pendellösung* fringes. Such fringes arise from dispersion-surface interbranch interference. Less familiar are intrabranch interference phenomena dependent upon the geometry of the crystal surfaces. Those in the latter class first to be explored experimentally are named after their discoverers (Borrmann & Lehmann, 1963; Lehmann & Borrmann, 1967).

In the early studies of Borrmann-Lehmann fringes the diffraction conditions corresponded to the high-absorption case, with $\mu_0 t > 10$, μ_0 being the normal X-ray linear absorption coefficient and t the crystal thickness. Thus, in the first experiments (Borrmann & Lehmann, 1963) the value of $\mu_0 t$ was 18 and in later experiments (Lehmann & Borrmann, 1967) it was 76. Accordingly, observations were confined to a very narrow central bundle of rays within the energy-flow triangle contained between the directions $\mathbf{K}_0$ and $\mathbf{K}_g$ subtending from the point of incidence on the crystal: only those rays travelling nearly parallel to the Bragg planes and for which anomalous transmission was strong could be photographed.

In the present work absorption was moderately low ($\mu_0 t = 1{\cdot}6$) or small ($\mu_0 t = 0{\cdot}47$), and rays spanning the whole opening angle of the energy-flow triangle were observed. We have made use of the continuous spectrum of synchrotron radiation to record fringe patterns at selected wavelengths, and the property of linear polarization of synchrotron radiation has been exploited to produce patterns with either σ-mode or π-mode polarizations alone. The latter was done both for the purpose of eliminating overlap of σ-mode and π-mode patterns and also to enable us to control the strength of scattering *via* the factor $|\cos 2\theta_B|$. The specimens we used were polished parallelepipeds of natural diamonds. One of these was deemed to be of sufficiently high long-range lattice perfection to be suitable for testing the usefulness of Borrmann-Lehmann fringe-spacing measurements to calculate F_g. The numerical values derived were disappointingly bad, but they pointed to a useful application of Borrmann-Lehmann fringe measurements in a quite different direction, that of serving as an extremely sensitive indicator of lattice distortion.

2. Diffraction geometry

Consider a crystal bounded by plane facets. Let $\mathbf{K}_0$ and $\mathbf{K}_g$ be the wave vectors of incident waves and of waves Bragg-diffracted by reflection g, respectively. (These vectors refer to wave directions outside the crystal. For present purposes their directions need not be distinguished from those of the corresponding crystal waves, $\mathbf{k}_0$ and $\mathbf{k}_g$, which are linked precisely by $\mathbf{k}_g = \mathbf{k}_0 + \mathbf{g}$.) For each facet, identified by its unit normal $\mathbf{n}$, a negative value of $(\mathbf{K}_0 . \mathbf{n})(\mathbf{K}_g . \mathbf{n})$ defines a 'Bragg surface', and a positive value a 'Laue surface' (and independently of whether $\mathbf{n}$ is defined as inward or outward drawn). When $(\mathbf{K}_0 . \mathbf{n})(\mathbf{K}_g . \mathbf{n})$ is positive at both X-ray entrance and exit surfaces of the specimen we have Laue-Laue diffraction, as in the familiar situation of a plate-shaped specimen when both $\mathbf{K}_0$ and $\mathbf{K}_g$ pass through the plate from one major surface to another. However, if the point of incidence of X-rays is moved towards an edge of the plate the energy-flow triangle may be cut by a lateral surface whose normal $\mathbf{n}$ makes $(\mathbf{K}_0 . \mathbf{n})(\mathbf{K}_g . \mathbf{n}) < 0$. We then have Laue-Bragg diffraction, at least in part of the energy-flow triangle (Saka, Katagawa & Kato, 1972*a*). Two Laue-Bragg situations have to be considered, depending upon whether the lateral surface cuts into the $\mathbf{K}_g$ side or the $\mathbf{K}_0$ side of the energy-flow triangle. They are shown in Figs. 1(*a*) and (*b*), respectively. The diagrams are drawn with the simplifying assumption that the section of the crystal by the plane of incidence is rectangular, and that the Bragg-diffracting planes are normal to the major faces of the plate (the 'symmetrical Laue case' for Laue-Laue diffraction). The patterns reproduced below were all obtained with such simple specimen geometry. An important parameter is the ratio of a, the distance of the point of incidence of X-rays from the edge of the crystal, to t, the crystal thickness. Obviously, Laue-Bragg diffraction conditions only come into play when $(a/t) < \tan \theta_B$.

A property of Bragg surfaces is that when the Poynting vector **s** of a Bloch wave in the crystal impinges upon a Bragg surface a significant fraction of its energy is reflected back into the crystal. Thus, in the situations shown in Fig. 1 [and more fully explained in Fig. 4(*a*)], rays may reach the Laue exit surface to the right of the corner *E* by two paths, one direct from the point of incidence of X-rays and the other *via* reflection at the lateral Bragg surface. The optical path difference between these rays produces the Borrmann–Lehmann fringes which can be observed in both the $\mathbf{K}_0$ and the $\mathbf{K}_g$ beams issuing from the crystal surface to the right of *E*. A complete theoretical treatment of the Laue–Bragg case has been presented by Saka, Katagawa & Kato (1972*a*). They call the diffraction geometry of Fig. 1(*a*) 'Type I', and that of Fig. 1(*b*) 'Type II'. We suggest that a more descriptive and easily remembered terminology is desirable. The significant action of the Bragg surface is partial reflection of the Poynting vector $\mathbf{s}_i$ impinging on it from within the crystal. Calling the reflected Poynting vector in the crystal $\mathbf{s}_r$, we have $\mathbf{s}_r = \mathbf{s}_i + \Delta\mathbf{s}$. In Fig. 1(*a*) $\Delta\mathbf{s} \cdot \mathbf{g}$ is negative, and in Fig. 1(*b*) $\Delta\mathbf{s} \cdot \mathbf{g}$ is positive. Accordingly, we propose that 'Type I' be termed the 'negative case', and 'Type II' the 'positive case'.

Some characteristics of Borrmann–Lehmann fringes are illustrated by the section topographs in Figs. 2 and 3. These were obtained with a conventional radiation source (Cu $K\alpha_1$) before the Synchrotron Radiation Source at Daresbury became operational. Fig. 2 is the $\mathbf{K}_g$-beam pattern taken in the negative setting, Fig. 1(*a*). Borrmann–Lehmann fringes appear to the right of the image of the edge *E*. Immediately to the left of *E* the $\mathbf{K}_g$ beam is relatively weak because of the partial internal reflection of the Poynting vector at the Bragg surface. (Note that the strong rise in intensity as the left-hand margin is approached occurs not just because the absorption path in the crystal is low there, but principally because the linear spread of a given angular fan of rays diverging from the point of incidence on the X-ray entrance surface is inversely proportional to the local crystal thickness.) Normal *Pendellösung* fringes can be seen, running vertically, between the image of *E* and the left-hand edge of the section. They appear very weakly in the right-hand part of the section; their visibility is poor compared with the Borrmann–Lehmann fringes seen close to *E*. No crystal-lattice dislocations are contained in the region of crystal included in the energy-flow triangle. The banded feature curving downwards on the right in the lower part of the pattern, which looks like the dynamical image of a dislocation, is in fact the dynamical image of the junction along a ⟨110⟩ direction of two adjacent {111} growth horizons within the crystal. Noteworthy is the non-uniformity of spacing of the Borrmann–Lehmann fringes: this varies more than twofold from top to bottom in the field reproduced. The diffraction geometry does not change from top to bottom, *i.e.* there is no change in *a* or *t*, so that crystal imperfections, superficial and

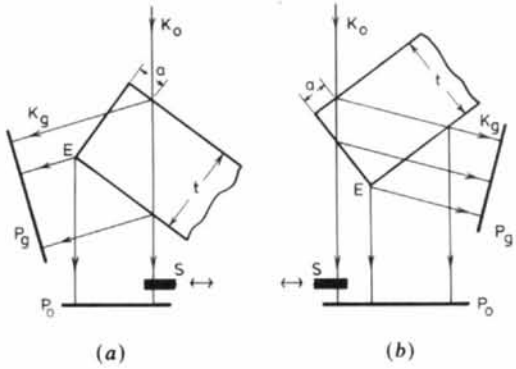

Fig. 1. Diffraction geometry for observing Borrmann–Lehmann interference phenomena. Parallelepiped-shaped crystal with faces normal to the plane of incidence. The Bragg-diffracting planes are normal to the Laue entrance surface and parallel to the lateral Bragg surface. Diffraction angles correspond to the 220 reflection of Cu $K\alpha_1$ by diamond, $2\theta_B = 75°$. P_0 and P_g are photographic plates set normal to the $\mathbf{K}_0$ and $\mathbf{K}_g$ beams, respectively. The screen *S* is movable as indicated by the double-headed arrows. With *S* withdrawn, the directly transmitted narrow ribbon incident beam is recorded on P_0. Borrmann–Lehmann interference fringes can be observed in both $\mathbf{K}_0$- and $\mathbf{K}_g$-beam images of the Laue exit surface to the right of the edge *E*. Crystal settings: (*a*) 'Type I', 'negative', (*b*) 'Type II', 'positive'.

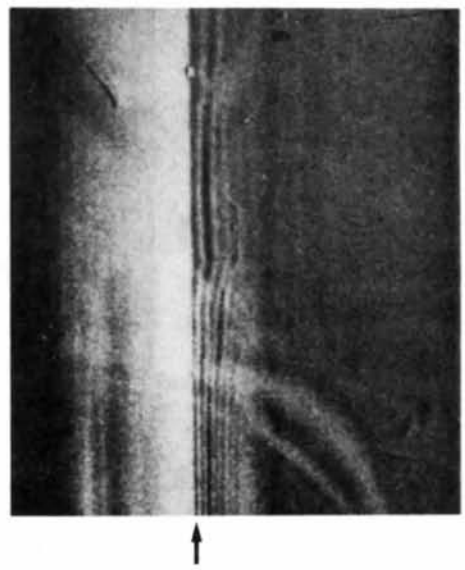

Fig. 2. $\mathbf{K}_g$-beam section topograph showing Borrmann–Lehmann fringes, negative setting (*cf.* Fig. 1*a*), Cu $K\alpha_1$ radiation, 220-type reflection. Arrow points to the image of the crystal edge *E*. Laue–Bragg conditions to the left of the arrow, Laue–Laue conditions to its right. Crystal thickness $t = 1$ mm ($\mu_0 t = 1{\cdot}6$), $a = 0{\cdot}18$ mm, width of section topograph image = 1·25 mm, full crystal height = 5 mm, but the image height reproduced here is 1·4 mm. (All topographs in the figures were recorded on Ilford L4 nuclear plates, emulsion thickness 25 μm.)

internal, are to be blamed for fringe-spacing inconstancy.

To illustrate the positive setting, Fig. 1(*b*), both a $\mathbf{K}_0$-beam image (Fig. 3*a*) and a $\mathbf{K}_g$-beam image (Fig. 3*b*) are shown. (The features arrowed are identified in the figure captions.) The same edge *E* of the same specimen appears in both Figs. 2 and 3. The average Borrmann-Lehmann fringe spacing in Fig. 3 is larger than in Fig. 2 because *a* is smaller, but the general patterns of fringe-spacing inconstancy are recognizably similar in the two settings. In $\mathbf{K}_0$-beam section topographs, the intensity tails off to zero at the margin of the pattern remote from the ribbon incident beam, as predicted by theory (Kato, 1960). This weak and featureless side of the section image has not been included in the field reproduced. Noteworthy in Fig. 3(*b*) is the strong image of the incident beam reflected from the Bragg surface. On the original plates it is seen that the strength and intensity profile of this image closely resemble those of the intense margins of a normal $\mathbf{K}_g$-beam section in the low and moderately low absorption cases. Consequently, it is easy to measure accurately the distance (*A*) on the plates between this Bragg-reflected beam and the Laue-Laue margin of the section topograph. Thus *a* may be accurately measured, *via* $a = \frac{1}{2}A \sec\theta_B$ with the present simple geometry. Comparison of $\mathbf{K}_0$ and $\mathbf{K}_g$ beam pairs in both positive and negative settings confirms that Borrmann-Lehmann fringe maxima in the $\mathbf{K}_0$ and $\mathbf{K}_g$ beams coincide in position along the exit surface, and that a minimum occurs at the edge *E*, in agreement with theory (Lehmann & Borrmann, 1967; Saka, Katagawa & Kato, 1972*a*, *b*).

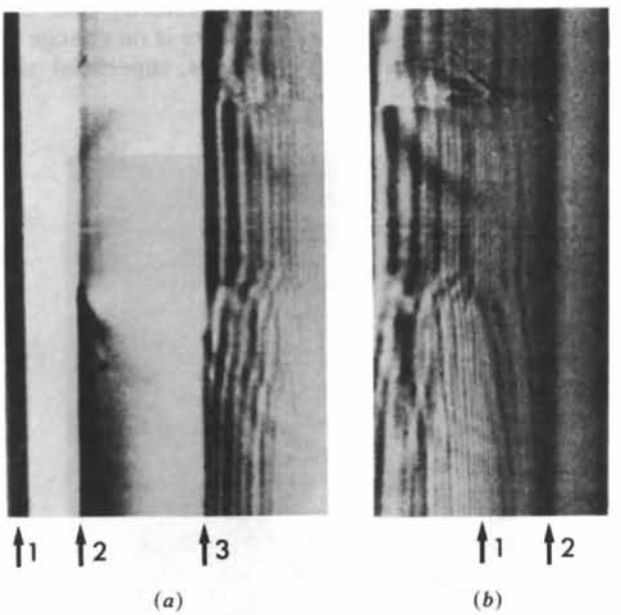

Fig. 3. Section topographs showing Borrmann-Lehmann fringes, positive setting (*cf.* Fig. 1*b*), Cu $K\alpha_1$ radiation, reflection inverse to that shown in Fig. 2. Specimen dimensions as in Fig. 2, but here $a = 0{\cdot}1$ mm. The height of image reproduced is 1·4 mm. (*a*) $\mathbf{K}_0$-beam image. The arrows numbered from left to right point to: (1) image of incident beam imprinted by brief removal of screen *S* (but broadened by heavy overexposure, the actual ribbon beam width being about 15 μm); (2) edge of shadow produced by *S*; (3) image of crystal edge *E*. (*b*) $\mathbf{K}_g$-beam image. The left-hand margin is the image of the crystal edge *E*. Arrows point to: (1) the point corresponding to the right-hand limit of the width of the $\mathbf{K}_0$-beam topograph printed in (*a*); (2) the internal Bragg reflection of the incident ribbon beam from the lateral Bragg surface, *i.e.* ray *PR'* in Fig. 4(*a*).

3. Simple theory

Fig. 4(*a*) shows the ray paths involved in Borrmann-Lehmann fringe formation. These are similar for the Type I, negative, and Type II positive settings; the latter is depicted in Fig. 4(*a*). For calculating fringe

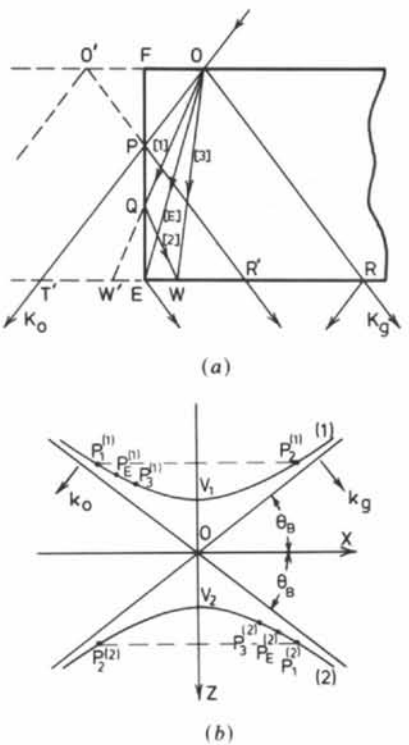

Fig. 4. (*a*) Ray paths involved in Borrmann-Lehmann interference in the Laue-Bragg case, positive setting (Type II). The ribbon incident beam enters the crystal at *O*. *W* is an observation point on the exit surface. Rays with directions between *OT'* and *OE* are reflected at the Bragg surface *FE* (which is also parallel to the Bragg planes) and appear to diverge from a source at *O'*, $FO = a$, $EW = b$. (Crystal thickness = *t*.) (*b*) Wavepoints on the dispersion surface corresponding to the rays shown in (*a*). Branches (1) and (2) drawn for a single polarization mode only. Poynting vectors $\mathbf{s}_1$, $\mathbf{s}_2$ *etc.* of rays [1], [2] *etc.* are normal to the dispersion surface at $P_1^{(i)}$, $P_2^{(i)}$ *etc.* ($i = 1$ or 2). The asymptotes to the dispersion-surface hyperbolae are intersections of the plane of incidence with spheres of radius *k*, the mean crystal wave vector; $k = K(1-\delta)$ where δ is the refractive index and $K = (\text{vacuum wavelength})^{-1}$. *OZ* lies in the Brillouin zone boundary, *OX* is parallel to **g**. The dashed lines through $P_1^{(i)}P_2^{(i)}$ are normals to the Bragg surface *FE*. (In the text the wave vector from *O* to the reciprocal-lattice origin is denoted by $\mathbf{k}_0^B$.)

spacings due to interference between waves following trajectory [1]+[2] and those following trajectory [3] the simple analysis given by Borrmann & Lehmann (1963) suffices. Fig. 4(*b*) shows the relevant wave points on the dispersion surface. For the high-absorption case Borrmann and Lehmann needed to consider only branch (1) and waves in the σ-polarization state. Here both branches (1) and (2) are considered, but only for a single polarization mode, in conformity with conditions applying in the synchrotron radiation experiments. For each ray drawn in Fig. 4(*a*), *i.e.* those identified as [1], [2], [3] and [*E*], the relevant wave points $P^{(1)}$ and $P^{(2)}$ on the dispersion surface branches, the Poynting vector **s**, the angle Θ between **s** and the Bragg plane, and the energy-flow parameter $p=\tan\Theta/\tan\theta_B$ are identified by subscripts. The angle Θ is conventionally taken as negative when **s** lies between the Bragg plane and $\mathbf{K}_0$, so that, with $FO=a$ and $EW=b$, $\tan\Theta_E=-a/t$ and $\tan\Theta_3=(b-a)/t$, for example. In the following elementary calculation the rectangular components X and Z of the difference between crystal wave vectors and the vector $\mathbf{k}_g^B=\mathbf{k}_0^B+\mathbf{g}$ at the Lorentz point O in Fig. 4(*b*) are employed. Since the Bragg surface is parallel to the Bragg reflecting plane, both X and the **g** component of the ray path reverse exactly after reflection. Hence to find the phase difference, S, between trajectory [1]+[2] and trajectory [3] one can simply compute the phase difference between trajectory [3] and trajectory [1] continued to W' on an assumed extended exit face. [This neglects the reversal of phase of the $\mathbf{k}_g$ wave on reflection, needed to satisfy the boundary conditions on the Bragg surface (Lehmann & Borrmann, 1967; Saka, Katagawa & Kato, 1972*a*).] For branch-(1) waves at W

$$S^{(1)}=2\pi t(|Z_3^{(1)}|-|Z_1^{(1)}|)-2\pi(a-b)|X_3^{(1)}| +2\pi(a+b)|X_1^{(1)}|. \quad (1)$$

From the symmetry of Fig. 4(*b*) it is apparent that the magnitudes of $S^{(1)}$ and $S^{(2)}$ are the same. Hence superscripts can be dropped, and calculation continued for branch (1) alone. In the coordinate system of Fig. 4(*b*) the dispersion-surface hyperbolae are given by

$$Z^2=X^2\tan^2\theta_B+(2\xi_g)^{-2}. \quad (2)$$

The diameter V_1V_2 is the reciprocal of the extinction distance ξ_g (the *Pendellösung* period parallel to the Bragg planes): $\xi_g^{-1}=(e^2/mc^2)(F_gC\lambda/\pi V\cos\theta_B)$, where C is the polarization factor and V the volume of the unit cell. For any Poynting vector **s**, $\tan\Theta=-\mathrm{d}Z/\mathrm{d}X$ and, from (2), $\tan\Theta=-X\tan^2\theta_B/Z$. With the assumption that b is small compared with a it is convenient to refer phases to that of ray [*E*] and to introduce $2\Delta X=X_1-X_3$, $2\Delta Z=Z_1-Z_3$, with $\Delta Z=-\tan\Theta_E\Delta X=(a/t)\Delta X$. Substitution in (1) gives simply

$$S=4\pi bX_E. \quad (3)$$

The proportionality of S to b shows that the fringes are equispaced along the exit surface close to E. Their spacing, Δ_a, on the exit surface is

$$\Delta_a=(2X_E)^{-1}. \quad (4)$$

If the deviation parameter $\omega=2\xi_g\tan\theta_BX$ and the relation $\omega^2=p^2/(1-p^2)$ are introduced, the right-hand side of (4) can be expressed in terms of $|p_E|=a/(t\tan\theta_B)$ and ξ_g. When p_E^2 is sufficiently small that one may put $\omega^2=p^2$,

$$\Delta_a=\xi_g\tan^2\theta_B(t/a), \quad (5a)$$

or

$$\Delta=\xi_g\sin\theta_B\tan\theta_B(t/a) \quad (5b)$$

when the fringe spacing $\Delta=\Delta_a\cos\theta_B$ on the photographic plate is measured. Equations (5) reproduce Borrmann & Lehmann's finding. Without the approximation applicable when p_E^2 is small,

$$\Delta_a=\xi_g\tan^2\theta_B(t/a)(1-p^2)^{1/2}. \quad (6)$$

The expression used for calculating F_g from Δ is

$$F_g=\left(\frac{mc^2\pi V}{e^2C\lambda}\right)\sin^2\theta_Bt(1-p^2)^{1/2}\left(\frac{1}{a\Delta}\right). \quad (7)$$

In their spherical-wave analysis of the Laue-Bragg case Saka, Katagawa & Kato (1972*a*) show that the Bragg-reflected waves behave as if they were diverging from a virtual source outside the crystal. In our simple geometry the virtual source is located at O' on OF prolonged, with $O'F=FO$. With this model of two energy-flow triangles overlapping, the similarity of contributions to the $\mathbf{K}_g$-beam image from rays OR and PR' in the positive setting [noted above in regard to Fig. 3(*b*)] is understandable. Furthermore, under low- and moderate-absorption conditions the *Pendellösung* fringe systems of the two energy-flow triangles overlap between E and R'. In fact, reference to Fig. 4(*b*) shows that for each polarization mode four periodicities should be recognizable in patterns produced by a perfect lightly-absorbing crystal: the Borrmann–Lehmann fringes, the two *Pendellösung* fringe systems, and the beat between the latter pair. In the patterns shown here, the calculated beat period between the *Pendellösung* fringe system was large close to E compared with the period of the first few Borrmann–Lehmann fringes measured. From the expressions given by Kato [1961, equation (55); 1974, equation (4-211*b*)] the *Pendellösung* fringe spacing at any point on the base of the energy-flow triangle in the symmetrical Laue–Laue case is easily calculated. At W, for example, the spacing on the exit surface due to the source at O is

$$\xi_gt\tan^2\theta_B(1-p_w^2)^{1/2}/|a-b|.$$

At E the fringe spacing of both *Pendellösung* fringe systems is

$$\xi_g \tan^2 \theta_B (1-p_E^2)^{1/2}(t/a),$$

just the same as the Borrmann-Lehmann fringe spacing, equation (6). The reason for this identity is apparent from Fig. 4(b). When W is close to E the difference between $[\mathbf{k}_g^{(1)}-\mathbf{k}_g^{(2)}]$ at E and W is $2P_E^{(i)}P_3^{(i)} = P_1^{(i)}P_3^{(i)}$. Of course whether the two *Pendellösung* fringe systems will reinforce or cancel each other in the vicinity of E depends upon the value of a.

4. Observations with synchrotron radiation

4.1. *Comparison of patterns obtained with* Cu $K\alpha_1$ *and with synchrotron radiation*

For the first few fringes, close to E, the fringe visibility is 100% in the $\mathbf{K}_g$ beam with the positive setting (Type II), and also 100% in the $\mathbf{K}_0$ beam in the negative setting (Type I). It is experimentally easier to record $\mathbf{K}_g$-beam patterns since the precisely positionable screen S is not required. In synchrotron-radiation experiments the Bragg reflection utilizes a much smaller fraction of the total energy of the X-ray spectrum of the source than when a characteristic radiation such as Cu $K\alpha_1$, produced in a conventional X-ray tube with a clean target and run at optimum kilovoltage, is being reflected. A practical consequence in experiments with white synchrotron radiation is that at diffraction angles close to $\mathbf{K}_0$ there is relatively more unwanted flux from scattering by air and slit jaws than in an equivalent conventional-source experiment. Therefore, recording of synchrotron-radiation $\mathbf{K}_0$-beam Borrmann-Lehmann fringe patterns has not been attempted to date, and experiments have been confined to the positive setting in order to obtain best fringe contrast in the $\mathbf{K}_g$ beam. Some experiments were performed with the same arrangement in plan as in Fig. 1(b) but with the specimen oriented so that the Bragg surface was not normal to the plane of incidence. In this case a varied linearly with distance normal to the plane of incidence. This geometry produced interestingly complex patterns, but the simple geometry of Fig. 1(b), with constant a for the whole crystal region imaged, was preferred for making fringe-spacing measurements.

The diamond which produced the images seen in Figs. 2 and 3 was the most perfect suitably faceted specimen available for the present study; but in these topographs departures from long-range lattice perfection were strongly evident. However, when set in a different orientation, using a {110} Bragg surface orthogonal to that effective in Figs. 2 and 3, highly regular patterns of both *Pendellösung* and Borrmann-Lehmann fringes were obtained which encouraged hope that reliable values of F_g might be extracted from the Borrmann-Lehmann fringe-spacing measurements. Typical patterns obtained in the new orientation are shown in Fig. 5: Cu $K\alpha_1$ in (a), synchrotron radiation, $\lambda = 1{\cdot}5$ Å, in (b). In this orientation the height of the crystal normal to the plane of incidence was 2 mm, and this full height appears in Fig. 5. The fringes are closely parallel over almost the whole height of the topographs. The values of $|p_E|$ were relatively high, so that the Borrmann-Lehmann fringe spacing was small. In both topographs about ten Borrmann-Lehmann fringes of high visibility run parallel to the left-hand margin of the image. They are shown in more detail in Figs. 6(a) and (b) where a 445 μm high segment of the left-hand part of each topograph is reproduced at higher magnification. Note that the overall image height in Fig. 5(a) is about 5% greater than in Fig. 5(b). This is due to the different ratios of distances between source and specimen, and specimen to plate, applying in the two experiments. In Fig. 5(a) the focus of the X-ray tube was only 450 mm from the specimen. In the synchrotron-radiation experiments the specimen was 80 m from the tangent point on the Storage Ring at

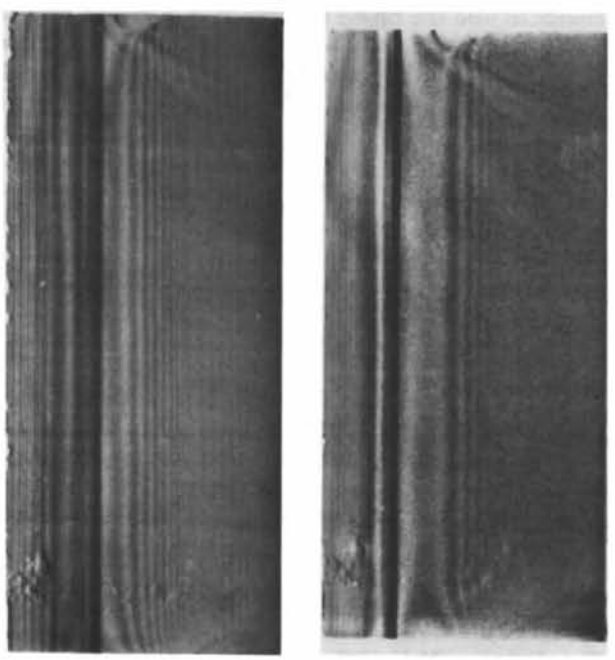

(a) (b)

Fig. 5. Comparison of Borrmann-Lehmann fringe patterns observed with (a) Cu $K\alpha_1$ radiation and (b) synchrotron radiation, $\lambda = 1{\cdot}5$ Å, σ-polarization mode. In these and subsequent figures the positive setting is employed, the crystal thickness is 1 mm, the left-hand margin of the topograph corresponds to the edge E of the crystal, and (except for Fig. 6) the full crystal height of 2 mm is included. Some indentation of the left-hand margin is caused by damage to the edge E. In (a), $|p_E| = 0{\cdot}49$, $a = 0{\cdot}38$ mm and in (b), $|p_E| = 0{\cdot}56$, $a = 0{\cdot}44$ mm.

the SERC Daresbury Laboratory, Warrington, Cheshire. There, with a specimen-to-plate distance of 30 mm, the vertical magnification departed from unity by less than 4 parts in 10^4. The slits close to the crystal defining the narrow ribbon incident beam had apertures between 10 and 15 μm in width in all experiments. At Daresbury the device designed for taking section topographs with synchrotron radiation (Lang, 1983) was used, mounted on the specimen axis of the white radiation camera (Bowen, Clark, Davies, Nicholson, Roberts, Sherwood & Tanner, 1982).

Another comparison of Cu $K\alpha_1$ and synchrotron-radiation fringe patterns is shown in Figs. 7(*a*) and (*b*). In this pair the values of a are closely similar, and are less than in the pair described above. Little difference between the Borrmann–Lehmann fringe patterns in Figs. 7(*a*) and (*b*) can be discerned. Images of internal lattice defects (*e.g.* the feature with mean height coordinate 0·78 in the left half of the image) and damage to the specimen surface (*e.g.* the patch centred on height coordinate 0·14 and fairly close to the left-hand margin) show identically in the two topographs. The dynamical feature that identifies the image taken with unpolarized Cu $K\alpha_1$ radiation is the periodic fading of *Pendellösung* fringe visibility evident between R' and R and due to the different fringe periods for the σ- and π-polarization modes (Hart & Lang, 1965; Hattori, Kuriyama & Kato, 1965).

4.2. *Variations of wavelength and polarization factor*

Experiments have been performed using continuous-spectrum synchrotron radiation to investigate the way diffraction contrast due to various types of crystal defect varies with wavelength in the range 0·57 to 2·5 Å when recorded on transmission topographs (Lang, Makepeace, Moore & Machado, 1983). The results highlighted the useful properties of radiation of wavelength about 1 Å, for which no strong conventional sources are available. Choice of this wavelength for Borrmann–Lehmann fringe observations was suggested by other considerations too. Firstly, the interest lay in Borrmann–Lehmann interference phenomena in the low-absorption case. This precluded use of a wavelength appreciably longer than 1·5 Å. Secondly, it was desired to retain a wide-section topograph image (to give a good field in which both Borrmann–Lehmann and *Pendellösung* fringes might be resolved) without having to increase the crystal thickness. This suggested setting $2\theta_B$ not less than ~45°, and hence λ not less than ~1 Å. (In the symmetrical Laue–Laue case, the section topograph image width is $2t \sin\theta_B$.) As regards changing the polarization factor, use was made of the facility offered by the white radiation camera at Daresbury for bodily rotation of collimation system, specimen axis and detector axis all together about the axis of the synchrotron beam line. With this facility, one can switch quickly between σ-polarization mode alone (plane of incidence on specimen normal to the storage-ring orbit plane) and π-polarization mode alone (plane of incidence parallel to the orbit plane) without changing any other adjustments.

Figs. 8(*a*) and (*b*) show Borrmann–Lehmann fringe patterns with the same specimen and similar diffraction geometry as in Figs. 5 and 7, but now taken with $\lambda = 1$ Å, and with σ polarization in (*a*) and π polariz-

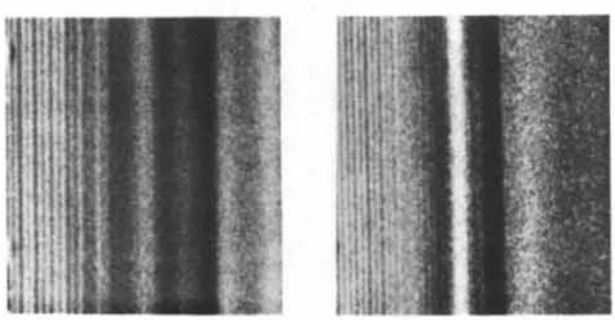

(*a*) (*b*)

Fig. 6. High-magnification illustrations of Borrmann–Lehmann fringes. Micrograph field width = 400 μm. (*a*) Part of Fig. 5(*a*), spacing of fringes near left-hand margin = 11 μm. (*b*) Part of Fig. 5(*b*), spacing of fringes near left-hand margin = 9·4 μm.

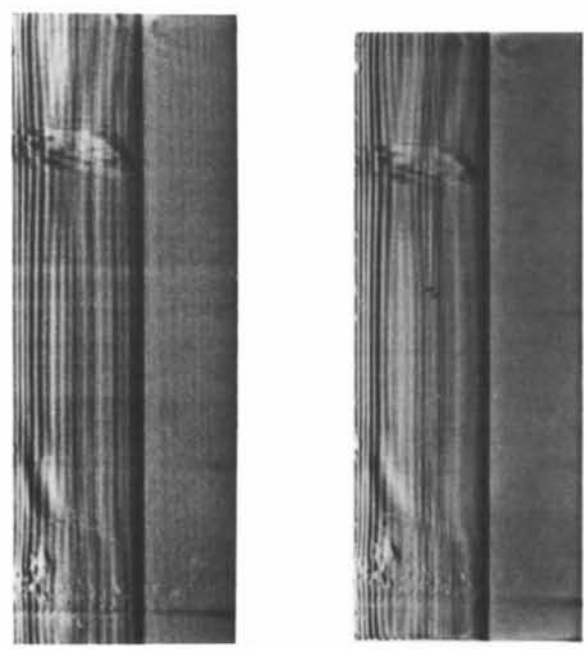

(*a*) (*b*)

Fig. 7. Borrmann–Lehmann fringe patterns typical of moderately low values of p_E. (*a*) Cu $K\alpha_1$ radiation, $|p_E| = 0{\cdot}27$, $a = 0{\cdot}21$ mm. (*b*) Synchrotron radiation, $\lambda = 1{\cdot}5$ Å, σ polarization, $|p_E| = 0{\cdot}26$, $a = 0{\cdot}20$ mm.

ation in (*b*). In comparing Fig. 8(*a*) with Fig. 8(*b*), note that there is only a small difference, about 12 μm, between the values of a in (*a*) and (*b*), so that differences between the patterns are mainly attributable to change of Δ rather than of a in the product $a\Delta$. There is an obvious difference between Figs. 8(*a*) and (*b*) in the pattern of irregularity of intensity and spacing of the Borrmann-Lehmann fringes. This is attributable more to a different pattern of interaction with lattice irregularities than of interaction with the *Pendellösung* fringe systems. Note also that there is no great difference in p_E between the patterns of Fig. 7 (mean $|p_E| = 0{\cdot}26$) and of Fig. 8 (mean $|p_E| = 0{\cdot}29$), and one might expect comparable fringe quality in these two figures. However, there is definitely a greater irregularity of Borrmann-Lehmann fringe spacing at the shorter wavelength. Inspection of the original plates also shows that the mean intensity in the image close to E relative to that in the region $R'R$ is less in the case of the shorter wavelength.

The effects of changing from σ to π polarization when $|\cos 2\theta_B|$ falls low are strikingly shown by Fig. 9. Here $|p_E| = 0{\cdot}22$, not greatly different from its value in Fig. 7. The calculated periods of both *Pendellösung* and Borrmann-Lehmann fringes are increased fourfold in Fig. 9 compared with Fig. 7(*b*). The consequent easier resolution of the *Pendellösung* fringes on the right-hand side of the image is evident. But in Fig. 9 the perturbation of the Borrmann-Lehmann fringes by lattice imperfections is so great as to render impossible the assignment of any definite period to these fringes. Also, the mean intensity between $p = p_E$ and $p \simeq 0$ is very weak relative to that in the rest of the pattern, and in comparison with the region near E in Figs. 5 and 7.

4.3. *Measurement of structure factor*

All the factors multiplying $(a\Delta)^{-1}$ in (7) are known, or are easily determinable when specimen and wavelength dependent. However, before we present the values of F_g obtained, a few remarks on instrumental factors which might possibly affect the observed resolution and spacing of fringes are called for. Firstly, one can dismiss variations of magnification factor normal to the plane of incidence (as discussed above in § 4.1) as being of any importance, since stretch of the image parallel to the image of the edge E has no effect on the fringe spacing. Next consider a standard calculation for geometrical resolution on a white-radiation topograph. The X-ray source dimensions at the tangent point on the storage ring are nominally 0·3 and 12 mm normal and parallel to the orbit plane, respectively. With the very large ratio of source-to-specimen (80 m) to specimen-to-photographic plate (30 mm) distances employed, the

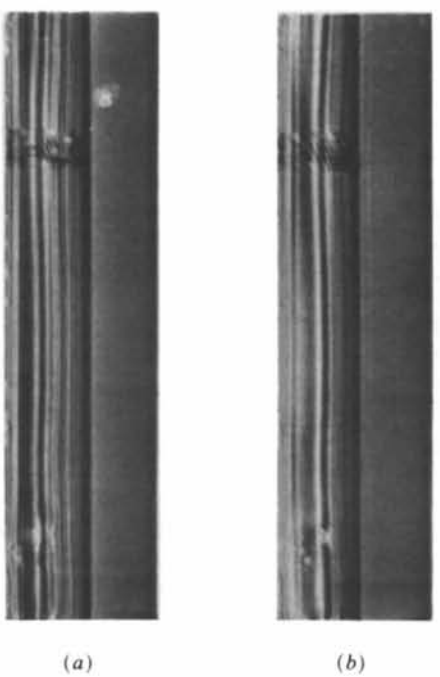

(*a*) (*b*)

Fig. 8. Synchrotron radiation Borrmann-Lehmann fringe patterns taken with $\lambda = 1{\cdot}0$ Å, $\theta_B = 23{\cdot}4°$, $\mu t = 0{\cdot}47$. (*a*) σ polarization, $|p_E| = 0{\cdot}28$, $a = 0{\cdot}12$ mm. (*b*) π polarization, $|p_E| = 0{\cdot}30$, $a = 0{\cdot}13$ mm.

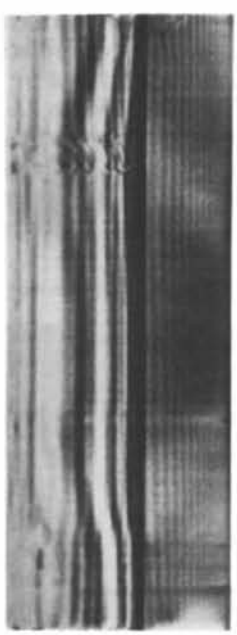

Fig. 9. Effect of low value $|\cos 2\theta_B|$ on Borrmann-Lehmann and *Pendellösung* fringe patterns. Synchrotron radiation, $\lambda = 1{\cdot}5$ Å, π polarization, $|\cos 2\theta_B| = 0{\cdot}254$, $|p_E| = 0{\cdot}22$, $a = 0{\cdot}17$ mm. Compare with Fig. 7.

Table 1. *Measurements of F_{220} from Borrmann–Lehmann fringe spacing*

Plate no.	Fig. no.	Radiation (λ, Å)	Polarization mode	a (mm)	Δ (μm)	$Ca\Delta$ (Å^2)	$\lvert p_E\rvert$	$(1-p_E^2)^{1/2}$	F(BLF)	F(BLF)/$F(D)$
3/5	5(*a*)	Cu $K\alpha_1$	$\sigma+\pi$	0·38	11	420	0·49	0·87	25·7	1·7
3/8	7(*a*)	Cu $K\alpha_1$	$\sigma+\pi$	0·21	23	480	0·27	0·96	24·6	1·6
40	5(*b*)	Syn. (1·5)	σ	0·44	9·4	410	0·56	0·83	24·9	1·6
41	—	Syn. (1·5)	σ	0·33	13	430	0·42	0·91	26·3	1·7
42	—	Syn. (1·5)	σ	0·23	21	480	0·29	0·95	24·8	1·6
44	7(*b*)	Syn. (1·5)	σ	0·20	23	460	0·26	0·97	26·1	1·7
45	—	Syn. (1·0)	σ	0·18	14	250	0·42	0·91	28·7	1·9
46	8(*a*)	Syn. (1·0)	σ	0·12	18	220	0·28	0·96	34·9	2·3
48	8(*b*)	Syn. (1·0)	π	0·13	23	210	0·30	0·95	37·1	2·4

calculated geometrical-optical blurrings of the X-ray image of a point on the crystal, in the two directions given, are 0·1 and 4·5 μm, respectively. Although the latter dimension is large from the point of view of X-ray topographic imaging of defects, it could only influence Borrmann–Lehmann fringe visibility in the π-polarization patterns, and is still small compared with the smallest fringe periods measured. Lastly, there is a significant difference to be noted in the effect the width of the beam-defining slit has on the visibility of *Pendellösung* compared with Borrmann–Lehmann fringes. Suppose this slit width is δ. Then, for symmetrical Laue-case diffraction conditions, the *Pendellösung* fringe visibility will fall to zero within such proximity to the section topograph margins that $\xi_g \tan\theta_B |p|^{-1}\ (1-p^2)^{1/2} \leq \delta$, applying the expression quoted in § 3 for *Pendellösung* fringe spacing on the X-ray exit surface. On the other hand, in Borrmann–Lehmann fringe patterns, the effect of finite slit width is to introduce uncertainty in the value of a, whereby the fringe visibility becomes impaired only when the fringe order is comparable with a/δ: fringes with periods smaller than δ can be well observed (*e.g.* Fig. 6*b*).

In Table 1 the values of the 220 structure factor found in the experiments here reported are listed in the column headed F(BLF). The last column contains the ratio F(BLF)/$F(D)$ where $F(D)$ is an accepted accurate value of F_{220}, 15·39, given by Dawson (1967). The table includes the measurable synchrotron radiation patterns illustrated in the figures, plus three more deemed of measurable quality. In the more distorted patterns the values assigned to Δ are very subjective, but no reasonable choice of Δ could bring F(BLF) substantially closer to $F(D)$. In the synchrotron radiation experiments the Bragg angle was set by rotation of the specimen from the zero value of θ_B established by optical reflection from the crystal face *ER* [indexed $(00\bar{1})$] viewed with an autocollimator aligned with the synchrotron beam axis. Departures of the polished specimen surfaces from the ideal orientations assumed in the analysis did not exceed about 1°, and could be ignored in view of the relatively large Bragg angles used and the large discrepancies, due to crystal imperfections, between experimental results and predictions of simple theory.

For comparison with the synchrotron radiation patterns, the findings on two Cu $K\alpha_1$ patterns illustrated are included. In these the dominant apparent fringe periodicity is that of the σ-polarization mode, and the value $C=1$ is adopted in the calculation of F(BLF). Examination of the plates shows that the F(BLF) values are much more in error than the values of F_{220} that would be derived from *Pendellösung* fringe-spacing measurements. Even in the case of Fig. 9, where no Borrmann–Lehmann fringe period can be assigned with any confidence, the *Pendellösung* fringes in the right-hand part of the image give an F_{220} value comparable with the best in the table.

5. Concluding remarks

In their pioneer experiments on a 12 mm thick silicon crystal with Mo $K\alpha$ radiation, Borrmann & Lehmann (1963) obtained agreement within ~25% between observed and calculated fringe spacings. Uragami (1971) has shown section topographs combining Laue–Laue and Laue–Bragg–Laue diffraction from a wedge-shaped silicon crystal with absorption paths ranging down to low values, but his complicated image geometry precludes easy comparison of observed with expected fringe periods. The evidence from our experiments is that comparing observed with calculated Borrmann–Lehmann fringe spacings is an extremely sensitive way of revealing lattice distortions. It deserves serious consideration as a practical crystal assessment technique, simpler to perform than double-crystal rocking-curve measurements. The advent of powerful synchrotron sources of continuous radiation extends the range of sizes and shapes of specimens with which Borrmann–Lehmann interference phenomena can be studied. The effects of epitaxial growth or ion implantation on the Bragg surface could be monitored non-destructively, possibly in real time.

The authors thank the Director and Staff of the SERC Daresbury Laboratory for the provision of experimental facilities, and SERC for financial support. The assistance of Professor Mai Zhenhong, Institute of Physics, Academia Sinica, Beijing, in obtaining the patterns shown in Figs. 2 and 3 is gratefully acknowledged.

References

BORRMANN, G. & LEHMANN, K. (1963). *Crystallography and Crystal Perfection*, edited by G. N. RAMACHANDRAN, pp. 101-108. London & New York: Academic Press.

BOWEN, D. K., CLARK, G. F., DAVIES, S. T., NICHOLSON, J. R. S., ROBERTS, K. J., SHERWOOD, J. N. & TANNER, B. K. (1982). *Nucl. Instrum. Methods*, **195**, 277-284.

DAWSON, B. (1967). *Proc. R. Soc. London Ser. A*, **298**, 264-288.

HART, M. & LANG, A. R. (1965). *Acta Cryst.* **19**, 73-77.

HATTORI, H., KURIYAMA, H. & KATO, N. (1965). *J. Phys. Soc. Jpn*, **20**, 1047-1050.

KATO, N. (1960). *Acta Cryst.* **13**, 349-356.

KATO, N. (1961). *Acta Cryst.* **14**, 627-636.

KATO, N. (1974). In *X-ray Diffraction*, by L. V. AZAROFF, R. KAPLOW, N. KATO, R. J. WEISS, A. J. C. WILSON & R. A. YOUNG, Ch. 4. New York: McGraw-Hill.

LANG, A. R. (1983). *Rev. Sci. Instrum.* **54**, 897-899.

LANG, A. R., MAKEPEACE, A. P. W., MOORE, M. & MACHADO, W. G. (1983). *J. Appl. Cryst.* **16**, 113-125.

LEHMANN, K. & BORRMANN, G. (1967). *Z. Kristallogr.* **125**, 234-248.

SAKA, T., KATAGAWA, T. & KATO, N. (1972*a*). *Acta Cryst.* A**28**, 102-113.

SAKA, T., KATAGAWA, T. & KATO, N. (1972*b*). *Acta Cryst.* A**28**, 113-120.

URAGAMI, T. S. (1971). *J. Phys. Soc. Jpn*, **31**, 1141-1161.

Acta Cryst. (1986). A**42**, 510-514

Determination of Phase Using Multiple-Beam Effects*

BY J. Z. TISCHLER

Solid State Division, Oak Ridge National Laboratory,† Oak Ridge, TN 37831, *USA*

AND B. W. BATTERMAN

School of Applied and Engineering Physics and Cornell High Energy Synchrotron Source, Cornell University, Ithaca, New York 14853, *USA*

(*Received* 17 *February* 1986; *accepted* 8 *May* 1986)

Abstract

It is shown that the absolute phase of a weak reflection can be obtained from an experimental integrated intensity measurement by taking into account multiple-beam effects. The absolute structure factor of the basis-forbidden 622 reflection in Ge has been measured. The contribution from weakly excited reflections whose phases are known acts as a reference wave for the reflection in question. It is further shown that, even in the limit of weak excitation of multiple beams, the intensity distribution in reciprocal space is determined by dynamical, not kinematical, theory. The remarkable result is demonstrated that several hundred beams are required to fully calculate X-ray multiple-beam effects, and an efficient approximation is presented for multiple-beam dynamical calculations with weak reflections. The intensity of weak multiple-beam effects, at least in the diamond structure, is roughly proportional to Z^4, where Z is the atomic number.

I. Introduction

X-ray scattering measurements can provide important information about the structure of crystalline materials. However, an unambiguous determination of structure requires knowledge of both the intensity and the phase of the scattered Bragg beams.

Generally, indirect phase information can be obtained through the use of a reference beam which is coherently related to the Bragg reflection being considered. One type of reference beam is created by the simultaneous excitation of a series of Bragg beams whose phases are known. The interaction of these multiple beams with the principal Bragg beam allows one to extract the phase of the principal beam.

In the present experiment we are interested in using the intensities and phases of weak quasi-forbidden reflections in the diamond structure to obtain detailed information about the charge distribution of valence electrons. The intensities, although quite weak, are measurable to fair accuracy using a synchrotron light source. We describe a method of measuring the absolute phase using many beam contributions from reflections far from the Ewald sphere. These extra beams are not negligible even under nominally optimized conditions, and affect the scattering in a way that allows one to extract the unknown phase.

The phases of the F's, the structure factors, for the allowed diamond-structure reflections are easily calculated from the known atomic positions. However, for basis-forbidden reflections ($h+k+l=4n+2$) it is the shape of the electron distribution around the nucleus that determines the value of F. For a spherical distribution, F is exactly zero. Thus for a

* The experimental work was part of a doctoral dissertation at Cornell Univ. See Tischler & Batterman (1984).

† Operated by Martin Marietta Energy Systems, Inc. under Contract No. DE-AC05-840R21400 for the US Department of Energy.

0108-7673/86/060510-05$01.50